Electrochemical reconstruction of metal-organic gels into crystalline oxy-hydroxide heterostructures for efficient oxygen evolution electrocatalysis

Kang Liu,[a] Haikuo Lan,[a] Yuting Chen,[a] Weicheng Tang,[a] Zhenyu Xiao,[a] Yunmei Du,[b] Jun Xing,[a] Zexing Wu,[a] Lei Wang,*[a]

a Prof. K. Liu, H. Lan, Y Chen, W. Tang, Prof. Z. Xiao, Prof. Y. Du, Prof. J. Xing, Prof. Z. Wu, Prof. L. Wang
Key Laboratory of Eco-chemical Engineering, International Science and Technology Cooperation Base of Eco-chemical Engineering and Green Manufacturing, College of Chemistry and Molecular Engineering, School of Materials Science and Engineering, Qingdao University of Science and Technology
Qingdao 266042, P. R. China
b Prof. Y. Du
College of Environment and Safety Engineering, Qingdao University of Science and Technology
Qingdao 266042, P. R. China

Email: inorchemwl@126.com

Material Preparation

Materials

The H_5L was drawn from previously reported literature.[1] KOH (99%), $CoCl_2 \cdot 6H_2O$ (99%), $FeCl_3 \cdot 6H_2O$ (99%) and $NiCl_2 \cdot 6H_2O$ (99%) were purchased from Aladdin. RuO_2 (99%), commercial 20% Pt/C and triethylamine (99%) were purchased from Macklin. Nafion™ perfluorinated resin solution (5 wt%) was purchased from Sigma-Aldrich. The electrodes used in the tests were purchased from Shanghai Chenhua Instruments. All reagents used were of analytical grade and did not require further purification.

Characterization instrumentation

X-ray diffraction (XRD) measurements were conducted using a Rigaku X-ray diffractometer. Fourier transform infrared (FT-IR) spectral data were obtained in the 4000-400 cm^{-1} range utilizing KBr particles on a Nicolet 460 spectrophotometer. The Brunauer-Emmett-Teller (BET) specific surface area was determined with using an ASAP 2460 instrument. X-ray photoelectron spectroscopy (XPS) analysis was carried out with an ESCALAB 250Xi instrument, where the spectrum was calibrated against the C 1s peak at 284.6 eV. Surface morphology and structure were characterized using a ZEISS Sigma 500 scanning electron microscope (SEM), JEM-ARM200F NEOARM atomic-level resolution transmission electron microscope (TEM) and high-resolution transmission electron microscopy (HRTEM) images were captured with a JEM2100UHR. Thermogravimetric analysis (TGA) was performed by heating the samples from 40 ℃ to 1000 ℃ at a rate of 10 ℃ min^{-1} using an STA 449 instrument. In-situ Raman spectra were recorded with a Raman spectroscopy system (Invia Qontor) using a 532 nm wavelength. The element distribution was characterized by ICP-MS2000B.

Electrochemical measurement

Weigh 5 mg of the prepared catalyst, add 600 μL of isopropanol and 400 μL of distilled water, and sonicate for 1 hour. Then, incorporate 20 μL of 5 wt% Nafion™ per fluorinated resin solution to create a uniform mixture of catalyst ink.

The preparation of the RuO_2 electrode follows the same procedure as the catalysts mentioned earlier.

Electrochemical tests were conducted using a CHI 760E electrochemical workstation with a three a three-electrode setup consisting of a polished glassy carbon electrode (GCE) (working electrode), a saturated calomel electrode (SCE) (reference electrode) and a platinum sheet (counter electrode) to evaluate the OER and HER performance of the catalysts in a 1 M KOH solution. On the central mirror of the GCE (3 mm in diameter), 5 μL of catalyst ink (loading of 0.35 mg cm^{-2}) was dropped and dried at room temperature. All potentials were converted to the reversible hydrogen electrode (RHE) via using the formula: $E_{RHE} = E_{SCE} + 0.059 * pH$. The polarization curve depicted in the figure was adjusted using another formula: $E_{C\text{orrect}} = E_{RHE} - IR\ (95\%)$, where I is the measured current and R is the resistance of the solution (~9.3 Ω).

Twenty cyclic voltammetry (CV) tests were conducted at a scan rate of 50 mV s^{-1} within the voltage range of 0~0.6 V to activate the electrode. The Linear sweep voltammetry (LSV) curve for OER was generated at a scan rate of 5 mV s^{-1} in an O_2-saturated 1 M KOH solution (1 M KOH solution saturated with N_2 for HER). Tafel plots were obtained by plotting (η) against the logarithm of current density (j) based on the LSV curves. The double-layer specific capacitance (C_{dl}) was calculated to estimate the electrochemically active surface area (ECSA) by performing CV tests at scan rates ranging from 2 to 10 mV s^{-1} within the non-Faraday region of 1.12~1.22 V. Electrochemical impedance spectra (EIS) were measured in the frequency range of 100 kHz~0.01 Hz at a current density of 10 mA cm^{-2} to determine the catalyst resistance. To evaluate overall water splitting, the catalyst ink was applied onto two pieces of nickel foam with equal loading, assembled into a two-electrode cell (cathode and anode), and tested in 1 M KOH solution. The total charge per unit time passing through the system was calculated using Faraday's law:

$Faradic\ efficiency = (nF \cdot m)/Q$,

$n = 4\ for\ OER (2\ for\ HER)$,

$F = 96485.3\ A\ s\ mol^{-1}$, $Q = It$.

Computational Methods:

Spin-polarized theoretical calculations were carried out with density functional theory (DFT) method as implemented in the Vienna Ab Initio Simulation Package (VASP).[2] The electron ion interaction was described with the projector augmented wave (PAW) method,[3] while the electron exchange and correlation energy were solved within the generalized gradient approximation with the revised Perdew-Burke-Ernzerhof (RPBE) exchange-correlation functional.[4-5] The empirical correction in Grimme's method (DFT+D3) was used to describe van der Waals interaction,[6] and the dipole correction was employed to correct potential spurious terms arising from the asymmetry of the slabs.[7] The kinetic energy cutoff of plane wave was set to be 500 eV and the convergence criterion for the residual forces and total energies were set to be 0.05 eV $Å^{-1}$ and 10^{-5} eV, respectively. A2×1 supercell slab of (100) edge was constructed containing four-atomic-layers. A vacuum layer of 25 Å was set between the periodically repeated slabs to avoid strong interactions and a 3×7×1 Monkhorst-Pack k-point grids was used to sample the Brillouin zone.

The Gibbs free energy change (ΔG) of each elementary step was calculated by using the computational hydrogen electrode (CHE) model proposed by Nørskov et al.[8] In this model, the chemical potential of the proton-electron pair in an aqueous solution is related to that of one-half of the chemical potential of an isolated hydrogen molecule. The ΔG value can be obtained by the formula: ΔG=ΔE+ΔZPE-TΔS, where ΔE is the reaction energy of reactant and product species adsorbed on the catalyst directly obtained from DFT calculations; ΔZPE and ΔS are the changes between the adsorbed species and the gas phase molecules in zero-point energies and entropy at 298.15 K, which can be calculated from the vibrational frequencies.

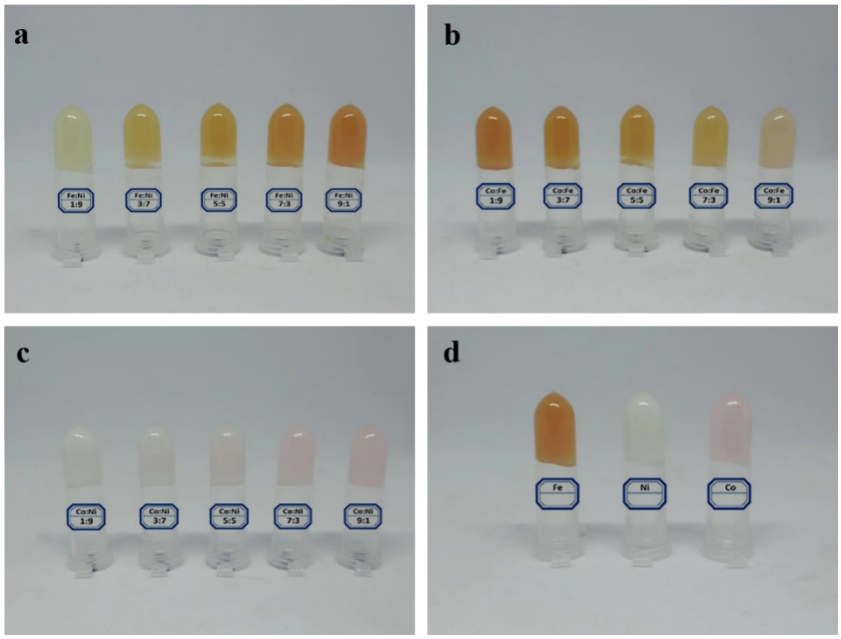

Fig. S1 Photograph of MOGs: a) Fe_1Ni_9~Fe_9Ni_1-MOG, b) Co_1Fe_9~Co_9Fe_1-MOG, c) Co_1Ni_9~Co_9Ni_1-MOG, d) Fe, Ni and Co-MOG.

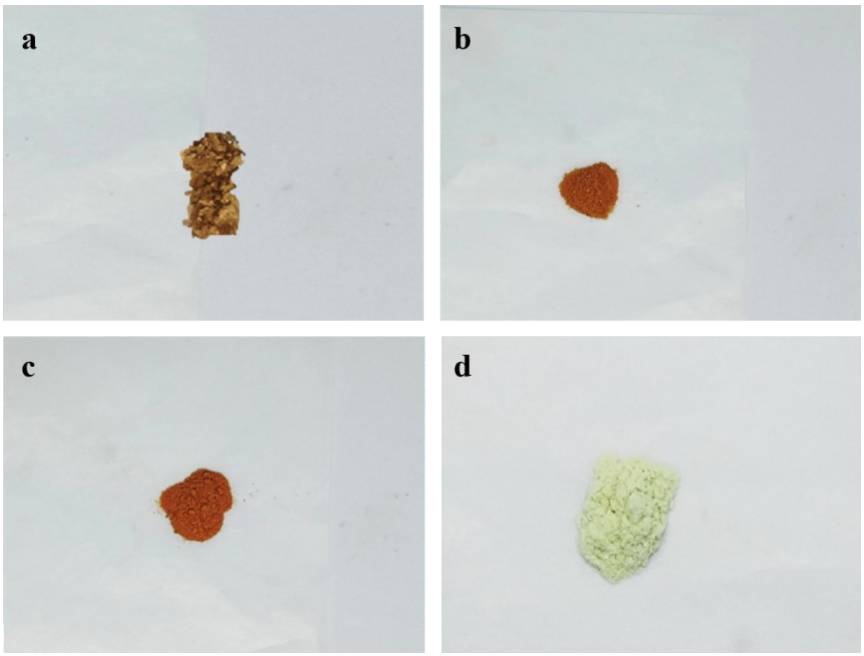

Fig. S2 Photograph of a) Re-Fe_5Ni_5-MOG, b) freeze-dried Fe_5Ni_5-MOG, c) freeze-dried Fe-MOG, d) freeze-dried Ni-MOG.

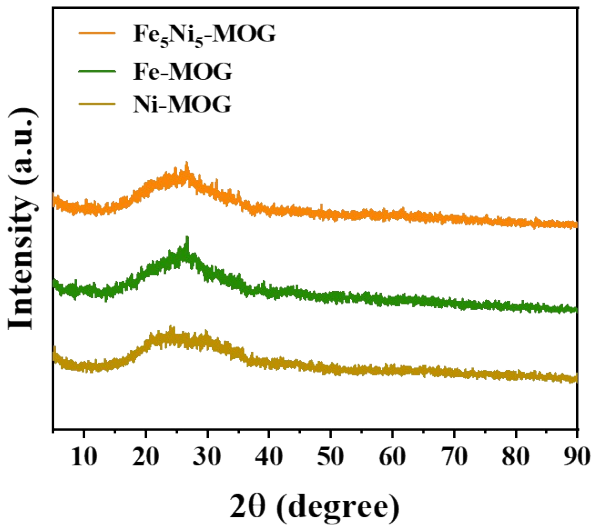

Fig. S3 XRD patterns of Fe_5Ni_5-MOG, Fe-MOG and Ni-MOG.

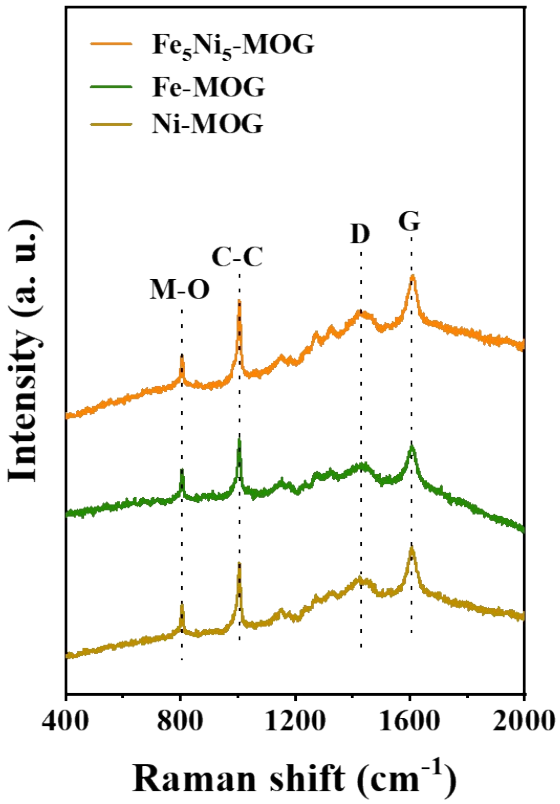

Fig. S4 The ex-situ Raman pattern of Fe_5Ni_5-MOG, Fe-MOG and Ni-MOG.

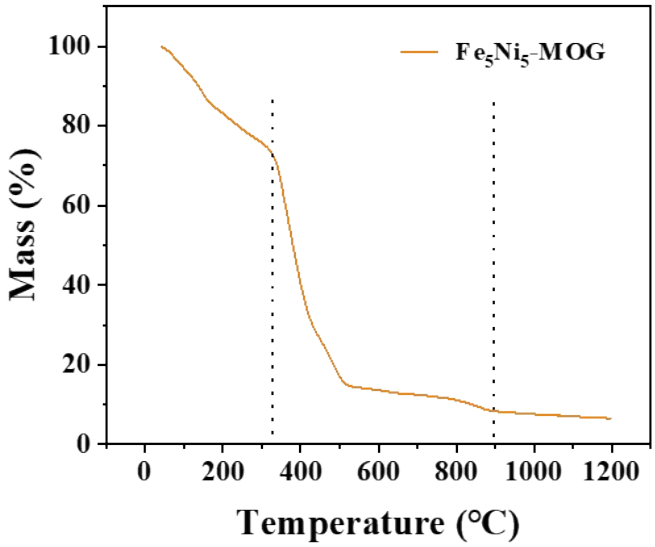

Fig. S5 TGA curves of Fe_5Ni_5-MOG.

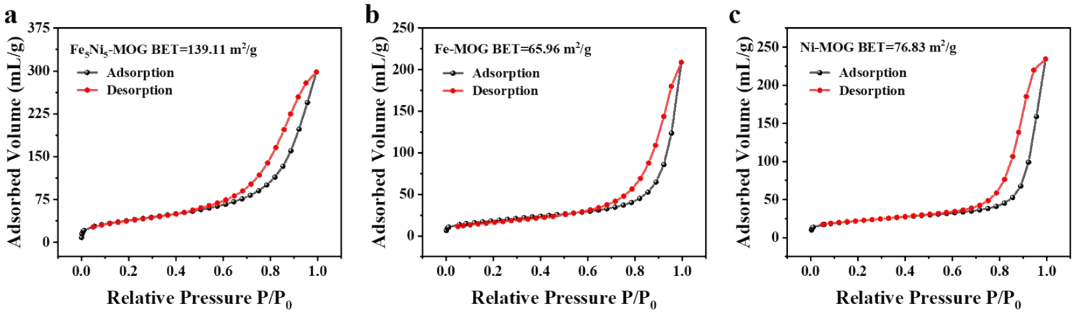

Fig. S6 N_2 adsorption-desorption isotherms of a) Fe_5Ni_5-MOG, b) Fe-MOG, c) Ni-MOG.

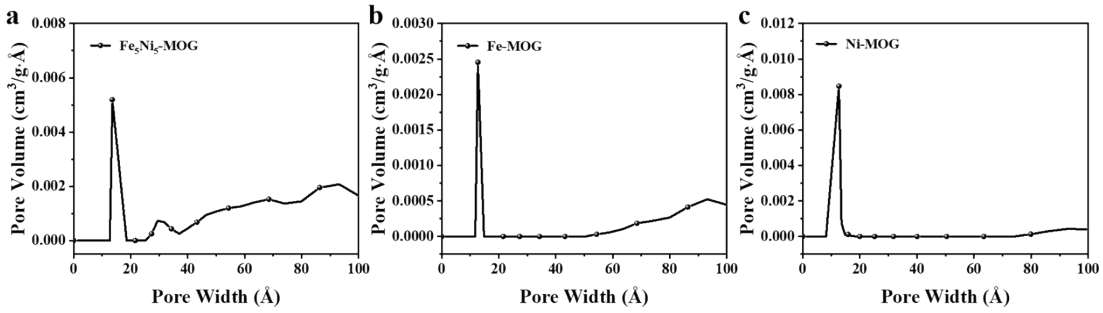

Fig. S7 Pore size distributions of a) Fe_5Ni_5-MOG, b) Fe-MOG, c) Ni-MOG.

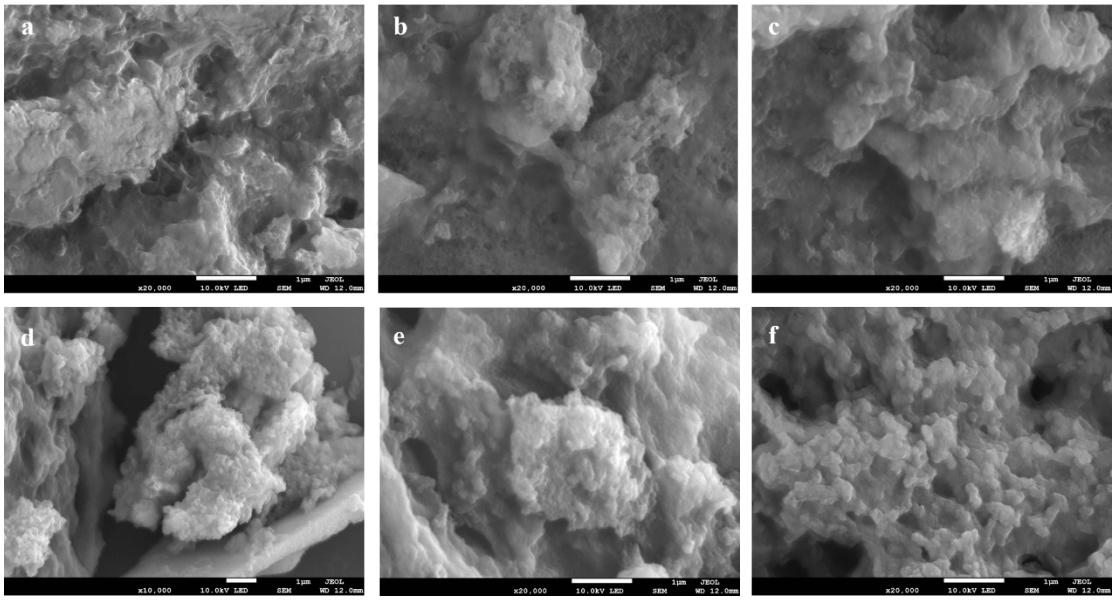

Fig. S8 SEM images with different magnifications of a-c) Fe-MOG, b-f) Ni-MOG.

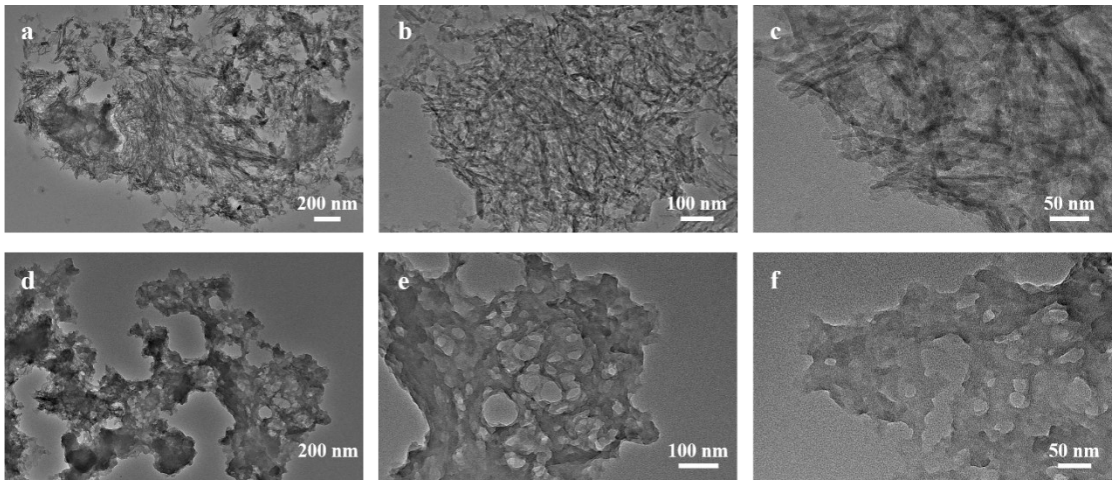

Fig. S9 TEM images with different magnifications of a-c) Fe-MOG, b-f) Ni-MOG.

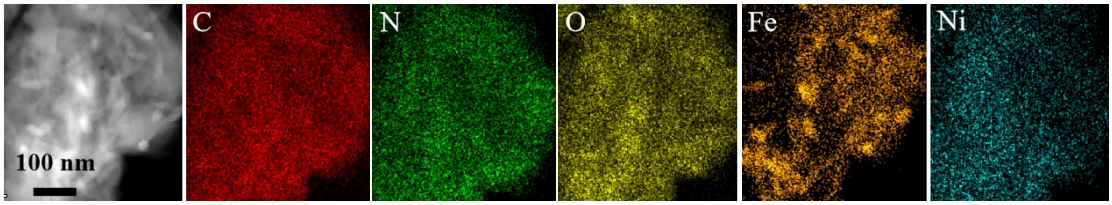

Fig. S10 HAADF-STEM image and corresponding elemental mapping images of Fe_5Ni_5-MOG. Scale bar: 100 nm.

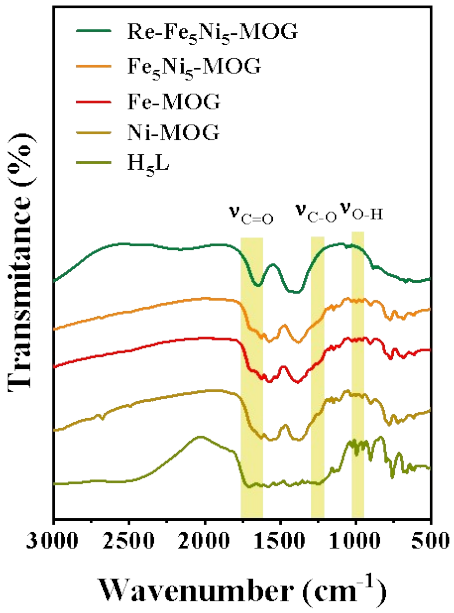

Fig. S11 FT-IR spectra of Re-Fe_5Ni_5-MOG, Fe_5Ni_5-MOG, Fe-MOG, Ni-MOG and H_5L.

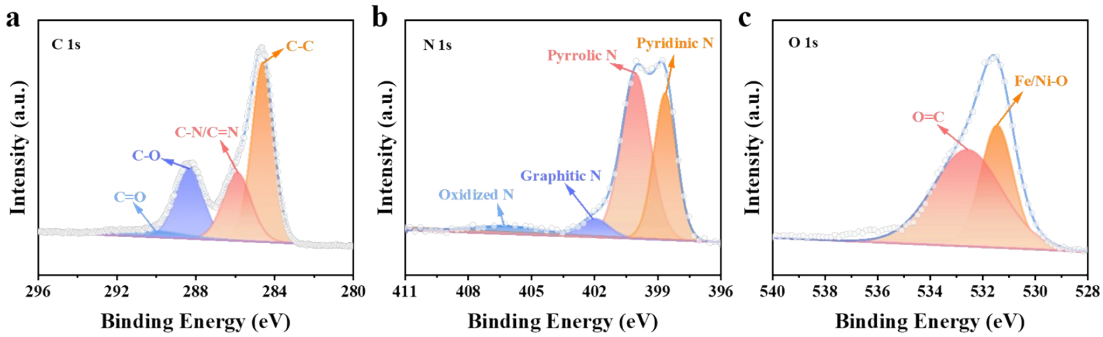

Fig. S12 High-resolution XPS spectra a) C 1s, b) N 1s, c) O 1s of Fe_5Ni_5-MOG.

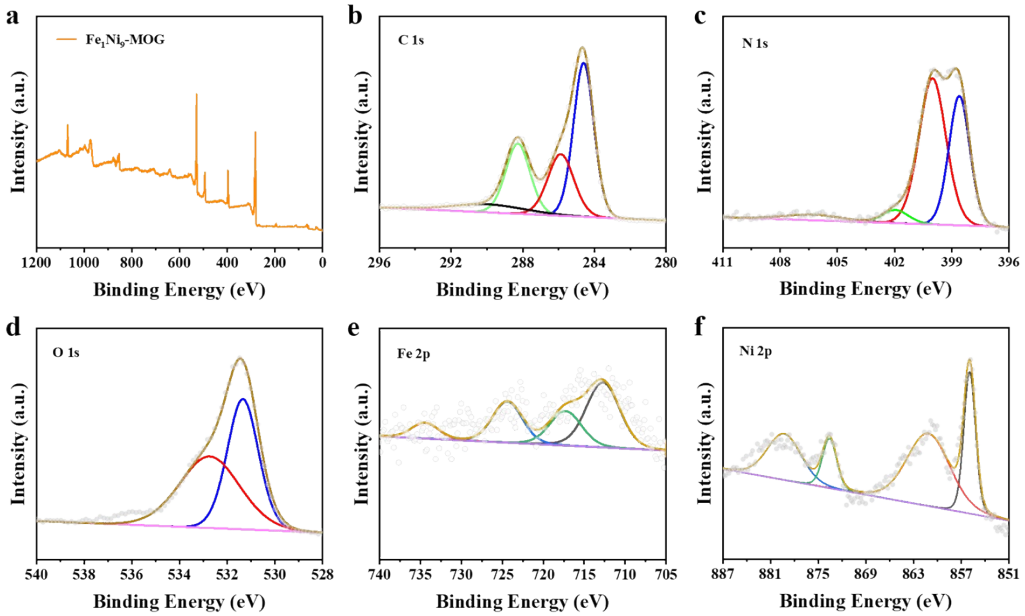

Fig. S13 a) High-resolution XPS full survey spectra of Fe_1Ni_9-MOG. b) C 1s, c) N 1s, d) O 1s, e) Fe 2p and f) Ni 2p of Fe_1Ni_9-MOG.

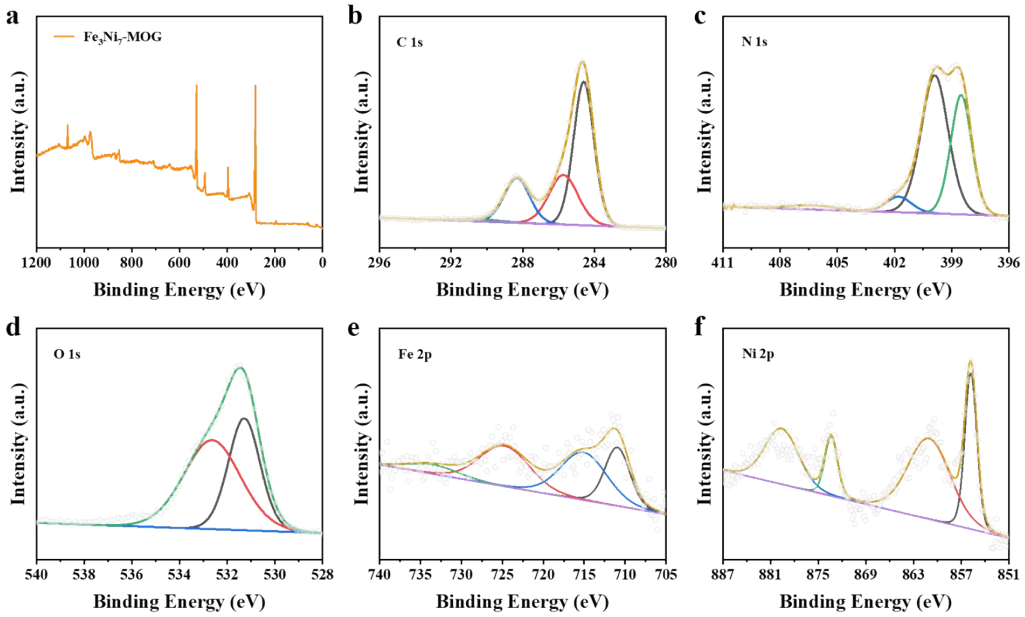

Fig. S14 a) High-resolution XPS full survey spectra of Fe_3Ni_7-MOG. b) C 1s, c) N 1s, d) O 1s, e) Fe 2p and f) Ni 2p of Fe_3Ni_7-MOG.

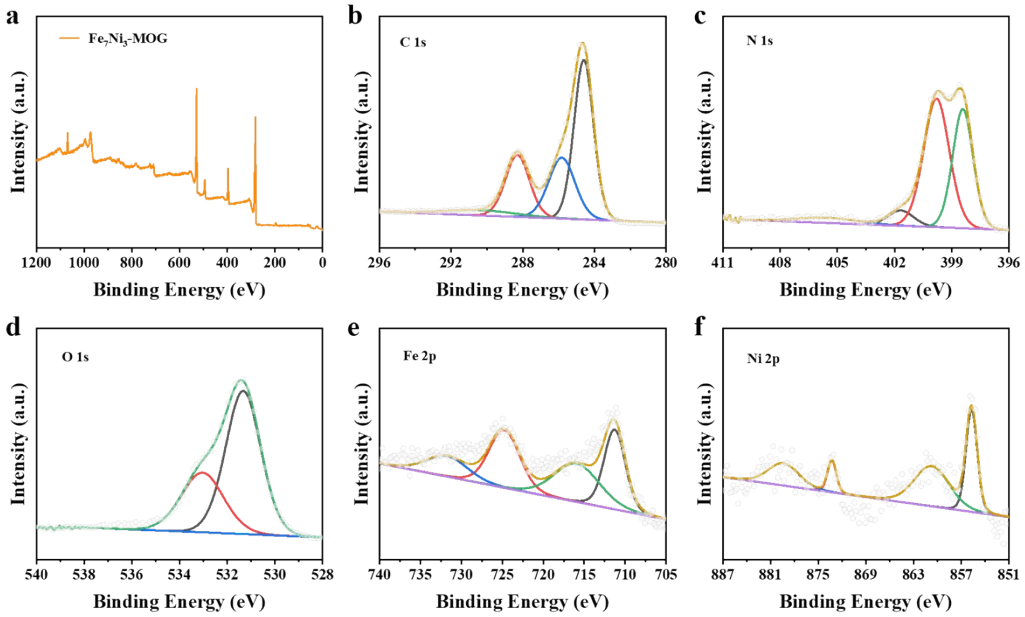

Fig. S15 a) High-resolution XPS full survey spectra of Fe_7Ni_3-MOG. b) C 1s, c) N 1s, d) O 1s, e) Fe 2p and f) Ni 2p of Fe_7Ni_3-MOG.

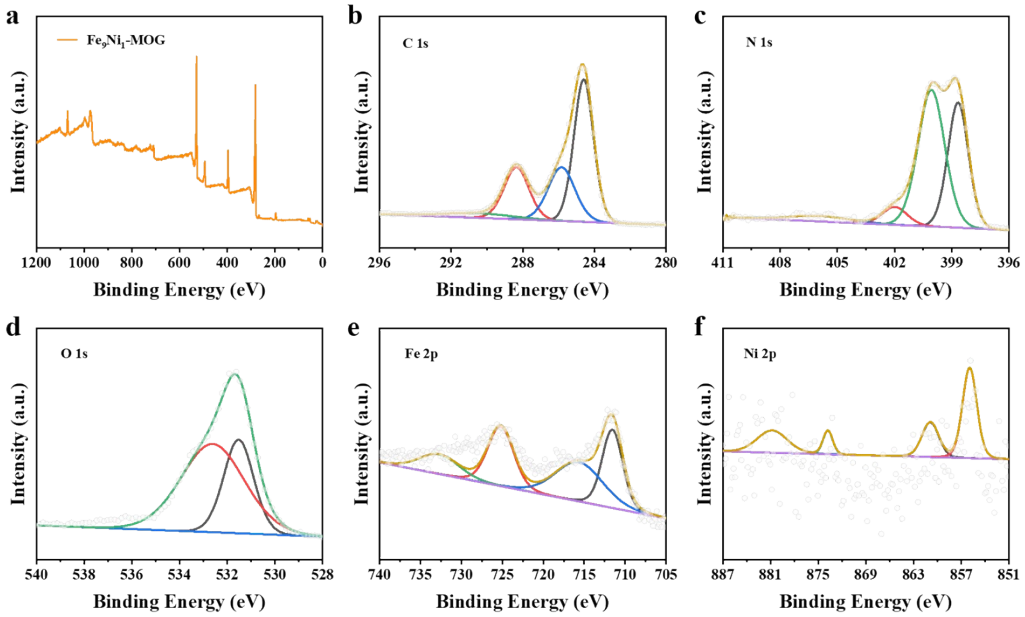

Fig. S16 a) High-resolution XPS full survey spectra of Fe_9Ni_1-MOG. b) C 1s, c) N 1s, d) O 1s, e) Fe 2p and f) Ni 2p of Fe_9Ni_1-MOG.

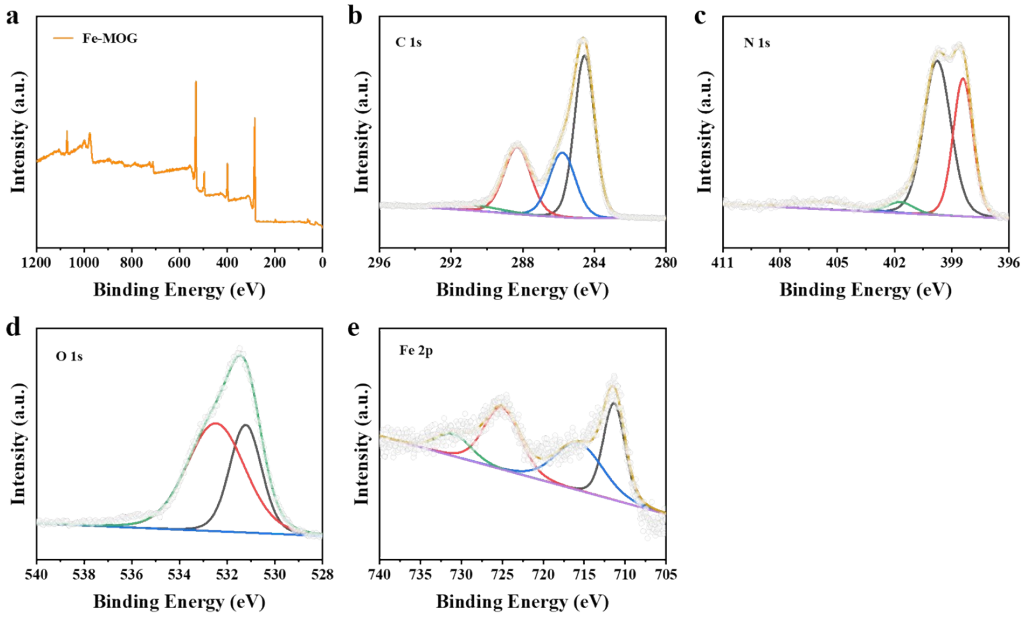

Fig. S17 a) High-resolution XPS full survey spectra of Fe-MOG. b) C 1s, c) N 1s, d) O 1s and e) Fe 2p of Fe-MOG.

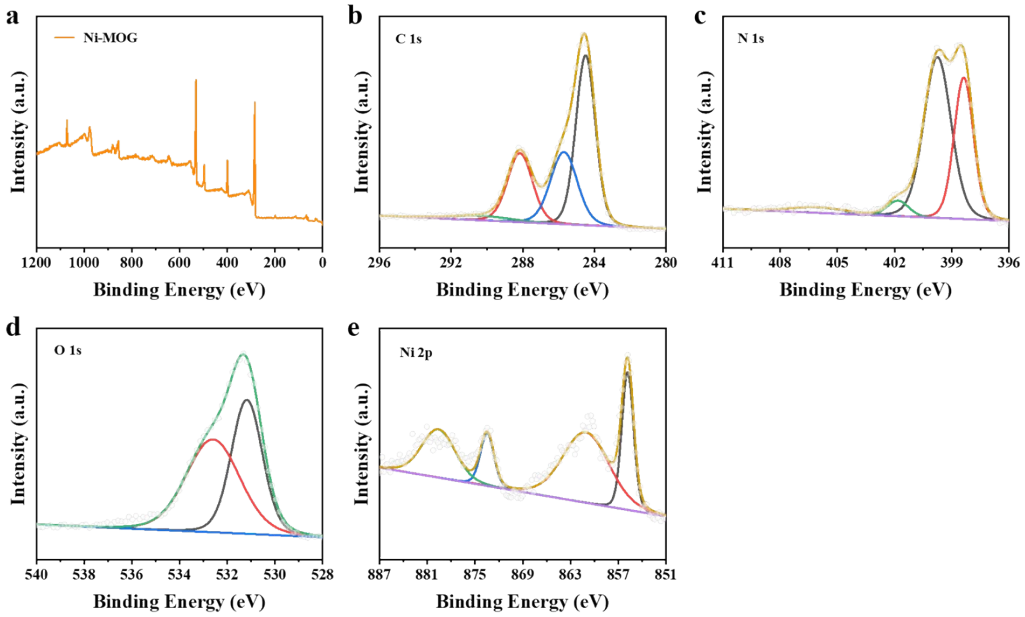

Fig. S18 a) High-resolution XPS full survey spectra of Ni-MOG. b) C 1s, c) N 1s, d) O 1s and e) Ni 2p of Ni-MOG.

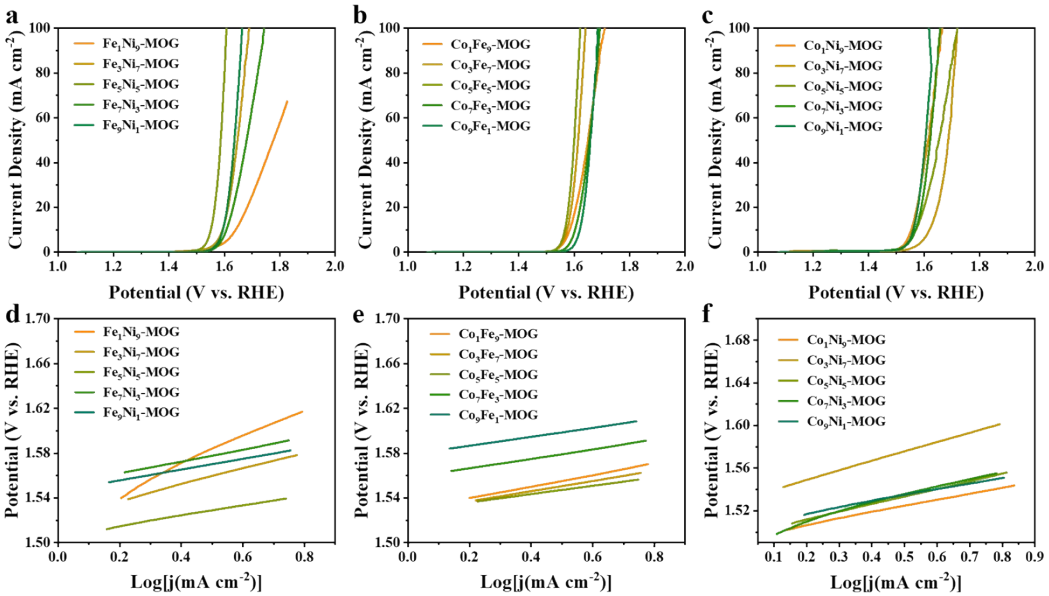

Fig. S19 LSV curves of a) Fe_1Ni_9~Fe_9Ni_1-MOG, b) Co_1Fe_9~Co_9Fe_1-MOG, c) Co_1Ni_9~Co_9Ni_1-MOG. Tafel plots of d) Fe_1Ni_9~Fe_9Ni_1-MOG, e) Co_1Fe_9~Co_9Fe_1-MOG, f) Co_1Ni_9~Co_9Ni_1-MOG.

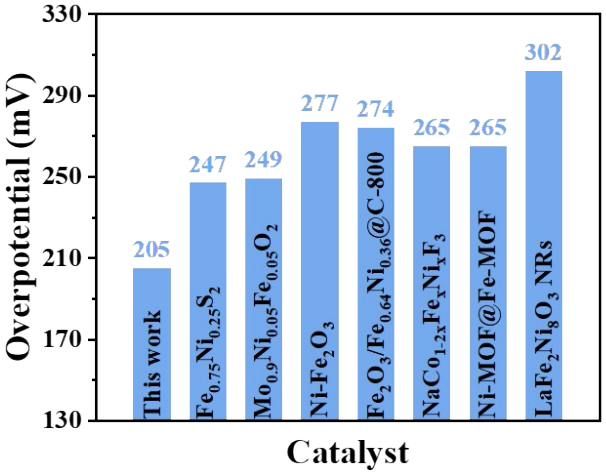

Fig. S20 Comparison for OER activity of Re-Fe_5Ni_5-MOG with some well-studied electrocatalyst in 1 M KOH.

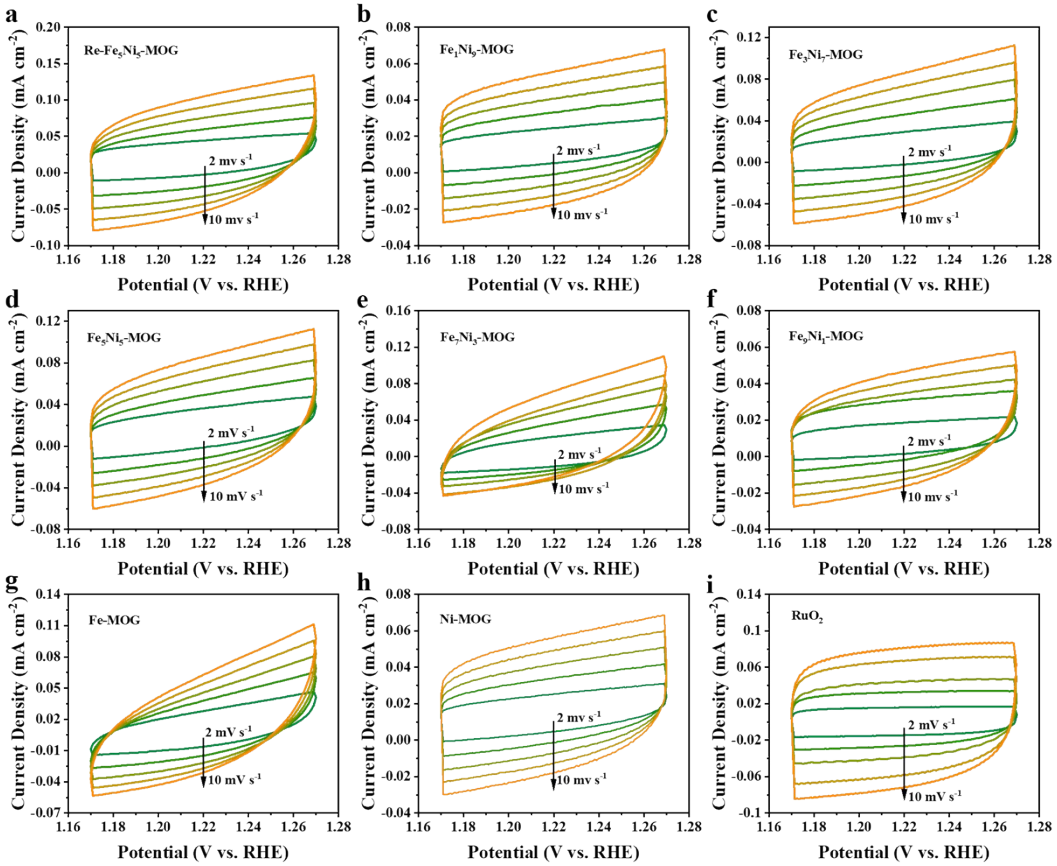

Fig. S21 CV curves at various scan rates (2~10 mV s^{-1}).

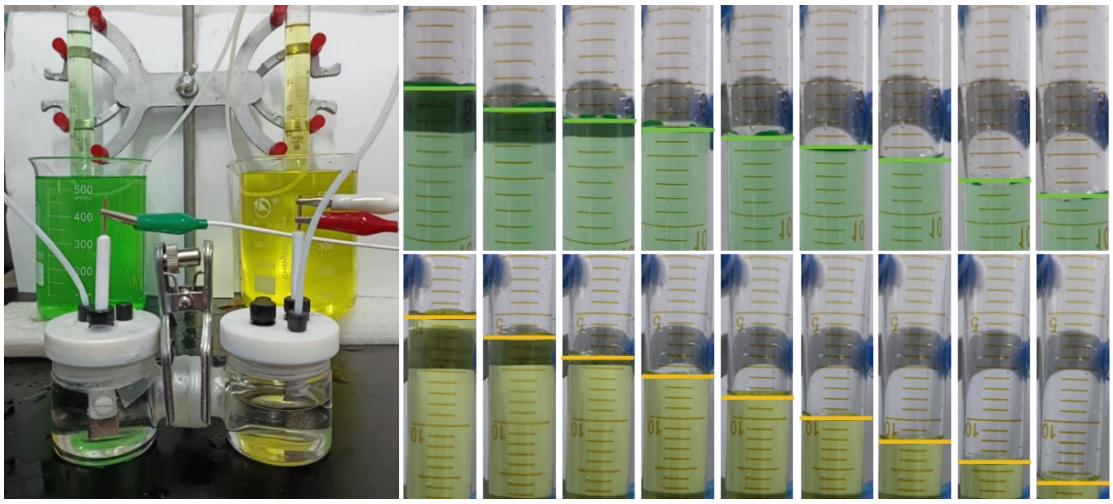

Fig. S22 Actual gas production using the drainage method during the overall water splitting (H_2 and O_2).

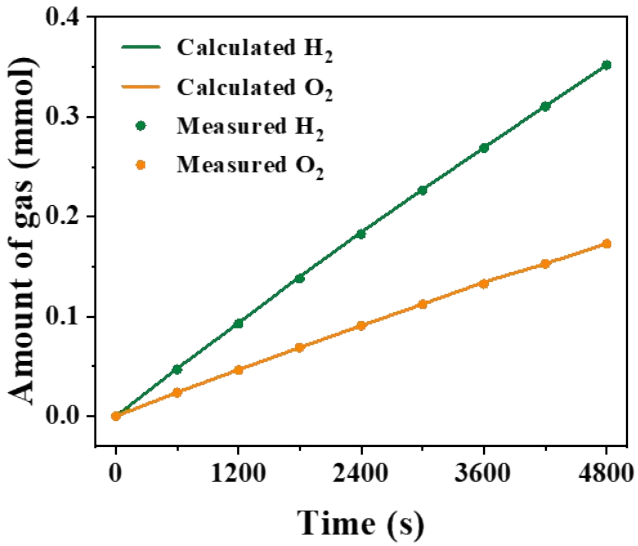

Fig. S23 Volume of Measured O_2, H_2 and calculated O_2, H_2 for Re-Fe_5Ni_5-MOG at the current density of 20 mA cm^{-2}.

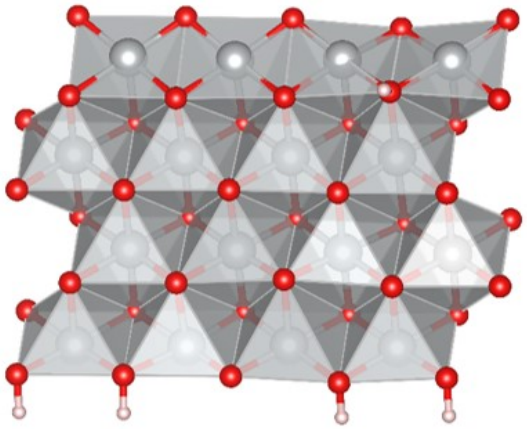

Fig. S24 Atomic model of NiOOH (Silvery balls: Ni atoms; Red balls: O atoms; White balls: H atoms).

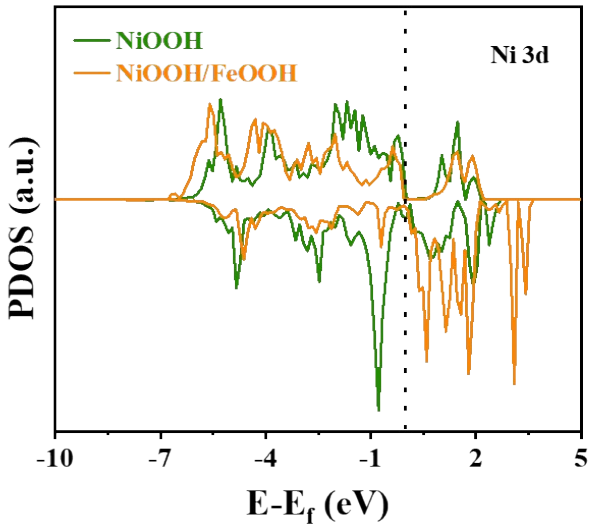

Fig. S25 The partial density of states (PDOS) of Ni 3d orbital for NiOOH and NiOOH/FeOOH.

$$H_2O + * \rightarrow OH* + H^+ + e^-$$
$$OH* \rightarrow O* + H^+ + e^-$$
$$O* + H_2O \rightarrow OOH* + H^+ + e^-$$
$$OOH* \rightarrow O_2 + H^+ + e^-$$

Fig. S26 Electron reaction paths for the single site of OER in NiOOH. Where * represents the active sites and OH*, O* and OOH* are the adsorbed intermediates.

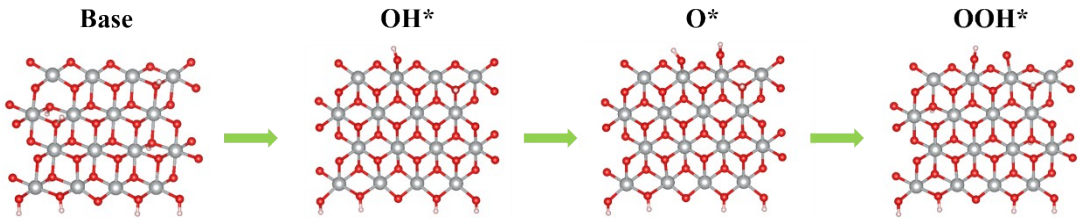

Fig. S27 Side view of the NiOOH model and the adsorbed OH*, O* and OOH* intermediates on the Ni site of NiOOH model (Silvery balls: Ni atoms; Red balls: O atoms; White balls: H atoms).

(a)

$Fe^* + Ni^* + H_2O \rightarrow Fe\text{-}OH^* + Ni^* + (H^+ + e^-)$

$Fe\text{-}OH^* + Ni^* + H_2O \rightarrow Fe\text{-}OH^* + Ni\text{-}OH^* + (H^+ + e^-)$

$Fe\text{-}OH^* + Ni\text{-}OH^* \rightarrow Fe\text{-}O^* + Ni\text{-}OH^* + (H^+ + e^-)$

$Fe\text{-}O^* + Ni\text{-}OH^* \rightarrow Fe^* + Ni^* + O_2 + (H^+ + e^-)$

(b)

$Fe^* + Ni^* + H_2O \rightarrow Fe\text{-}OH^* + Ni^* + (H^+ + e^-)$

$Fe\text{-}OH^* + Ni^* + H_2O \rightarrow Fe\text{-}OH^* + Ni\text{-}OH^* + (H^+ + e^-)$

$Fe\text{-}OH^* + Ni\text{-}OH^* \rightarrow Fe\text{-}OH^* + Ni\text{-}O^* + (H^+ + e^-)$

$Fe\text{-}OH^* + Ni\text{-}O^* \rightarrow Fe^* + Ni^* + O_2 + (H^+ + e^-)$

(c)

$Fe^* + Ni^* + H_2O \rightarrow Fe^* + Ni\text{-}OH^* + (H^+ + e^-)$

$Fe^* + Ni\text{-}OH^* + H_2O \rightarrow Fe\text{-}OH^* + Ni\text{-}OH^* + (H^+ + e^-)$

$Fe\text{-}OH^* + Ni\text{-}OH^* \rightarrow Fe\text{-}O^* + Ni\text{-}OH^* + (H^+ + e^-)$

$Fe\text{-}O^* + Ni\text{-}OH^* \rightarrow Fe^* + Ni^* + O_2 + (H^+ + e^-)$

(d)

$Fe^* + Ni^* + H_2O \rightarrow Fe^* + Ni\text{-}OH^* + (H^+ + e^-)$

$Fe^* + Ni\text{-}OH^* + H_2O \rightarrow Fe\text{-}OH^* + Ni\text{-}OH^* + (H^+ + e^-)$

$Fe\text{-}OH^* + Ni\text{-}OH^* \rightarrow Fe\text{-}OH^* + Ni\text{-}O^* + (H^+ + e^-)$

$Fe\text{-}OH^* + Ni\text{-}O^* \rightarrow Fe^* + Ni^* + O_2 + (H^+ + e^-)$

Fig. S28 Possible response pathways for the dual sites of OER in NiOOH/FeOOH: (a) pathway 1, (b) pathway 2, (c) pathway 3 and (d) pathway 4. Where * represents the active site and OH*, (OH*+OH*), and (O*+OH*) are adsorbed intermediates.

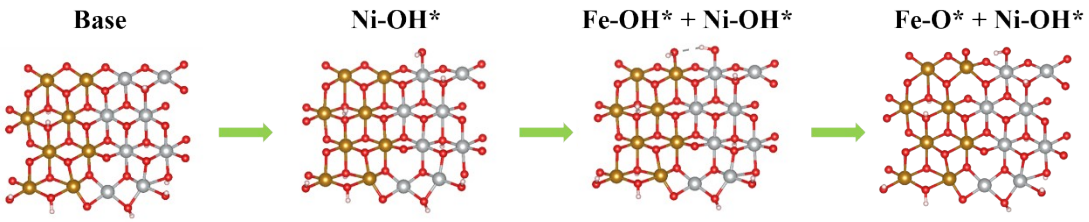

Fig. S29 Side view of the NiOOH/FeOOH model and the adsorbed OH*, O* and OOH* intermediates on the Fe-Ni dual site 2 of NiOOH/FeOOH model (Silvery balls: Ni atoms; Brown balls: Fe atoms; Red balls: O atoms; White balls: H atoms).

TOF：

According to the following formula, we have calculated the number of active sites:

$$\left(\frac{5\times 0.005\times 4.59\%\times 10^{-3}mg}{55.8g/mol}+\frac{5\times 0.005\times 4.22\%\times 10^{-3}mg}{58.7g/mol}\right)$$
$$\times 6.02\times 10^{23}\frac{1}{mol}=2.32\times 10^{16}sitescm^{-2}$$

According to the following formula, we have calculated the amount of hydrogen turnover from OER current density:

$$O_2=\left(j\frac{mA}{cm^2}\right)\left(\frac{1C/s}{1000mA}\right)\left(\frac{1mole^{-1}}{96485.3C}\right)\left(\frac{1molH_2}{4mole^{-1}}\right)\left(\frac{6.02\times10^{23}moleculesH_2}{1molH_2}\right)=1.56\times10^{15}\frac{H_2/s}{cm^2}per\frac{mA}{cm^2}$$

For OER：at the overpotential of 300 mV, the calculated TOF value was：

$$TOF=\frac{1.56\times 10^{15}\frac{H_2/s}{cm^2}per\times 57.04\frac{mA}{cm^{-2}}}{2.32\times 10^{16}sitescm^{-2}}=3.84s^{-1}$$

Tabel S1 Content of elements in ICP of Fe_5Ni_5-MOG samples.

Element	Content（%）
Fe	**4.586**
Ni	**4.218**

Table S2 Comparison for OER activity of catalysts of some OER electrocatalysts already reported and our work (1 M KOH).

Reference	Sample	η_{10} (mV)	Tafel slope (mV dec^{-1})	BET (m^2 g^{-1})	Substrate
This work	Re-Fe_5Ni_5-MOG	205	58	139.11	GCE
9	NiFe-LDH	350	47	60	GCE
10	$Co_{0.5}V_{0.5}$@COF-SO_3	318	62	184	CFP
11	Co-Mac-1	320	54	40.2	CFP
12	$CCOP_{TDP}$-FeNi-SiO_2	310	57	-	RRDE
13	NiFe-$NiCoO_{2.0}$	286	49.3	-	CFP
14	NiFe NRAs	305	54	14.42	Ni NRAs
15	FeCoNi $MnO_{2.0}$/CFP	390	104.4	-	CFP
16	CoNi@$Fe(OH)_3$-NF	310	106.4	-	NF
17	15% PANI/ZIF-67	340	37	-	RDE
18	PHI-$Co_{0.5}$	324	44	-	RDE
19	$A_{2.7}$B-MOF-$FeCo_{1.6}$	288	39	-	GCE

Table S3 Comparison for turnover frequency (TOF) of some OER electrocatalysts

already reported and our work (1 M KOH).

Reference	Sample	Overpotential (mV)	TOF (s^{-1})
This work	Re-Fe_5Ni_5-MOG	205	3.84
20	a-NiFeOOH/N-CFP	270	0.99
21	CoO@NiFe LDH/NF	350	0.59
22	FeCoNiP	350	0.95
9	NiFe-LDH	300	0.08
10	$Co_{0.5}V_{0.5}$@COF-SO_3	300	0.098

Table S4 The free energy change (△G) of each elementary reaction for OER on different catalysts.

Models	Sites	△G1 (eV)	△G2 (eV)	△G3 (eV)	△G4 (eV)
NiOOH	Ni site	1.58	1.56	1.81	-0.03
NiOOH/	Fe-Ni dual site 1	1.06	1.38	1.54	0.93

FeOOH	**Fe-Ni dual site 2**	**1.34**	**1.10**	**1.54**	**0.93**

References

1 Y. X. Wang, Z. Y. Li, J. Zhu, X. Q. Wang, L. L. Xu, A. Lachgar, J. J. Zhang, CrystEngComm, 2013, **15**, 6395-6402.

2 G. Kresse, J. Furthmüller, Phys. Rev. B, 1996, **54**, 11169.

3 P. E. Blöchl, Phys. Rev. B, 1994, **50**, 17953-17979.

4 B. Hammer, L. B. Hansen, and J. K. Nørskov, Phys. Rev. B, 1999, **59**, 7413-7421.

5 J. P. Perdew, K. Burke, M. Ernzerhof, Phys. Rev. Lett., 1996, **77**, 3865-3868.

6 L. Goerigk, S. Grimme, Phys. Chem. Chem. Phys., 2011, **13**, 6670-6688.

7 J. Neugebauer, M. Scheffler, Phys. Rev. B, 1992, **46**, 16067.

8 J. K. Nørskov, J. Rossmeisl, A. Logadottir, L. Lindqvist, J. R. Kitchin, T. Bligaard, H. Jónsson, J. Phys. Chem. B, 2004, **108**, 17886-17892.

9 K. Yan, T. Lafleur, J. Chai, C. Jarvis, Electrochem. Commun., 2016, **62**, 24-28.

10 Z. Gao, Z. Yu, Y. Huang, X. He, X. Su, L. Xiao, Y. Yu, X. Huang, F. Luo, J. Mater. Chem. A, 2020, **8**, 5907-5912.

11 Q. Liu, Q. Wang, J. Wang, Z. Li, J. Liu, X. Sun, J. Li, Y. Lei, L. Dai, P. Wang, Adv. Funct. Mater., 2020, **30**, 2000593.

12 J. Guo, T. Li, Q. Wang, N. Zhang, Y. Cheng, Z. Xiang, Nanoscale, 2019, **11**, 211-218.

13 R. Shi, J. Wang, Z. Wang, T. Li, Y. Song, Journal of Energy Chemistry, 2019, **33**, 74-80.

14 Y. Yan, H. Liu, C. Liu, Y. Zhao, S. Liu, D. Wang, M. Fritz, A. Ispas, A. Bund, P. Schaaf, X. Wang, Applied Materials Today, 2021, **25**, 101185.

15 Z. Ye, T. Li, G. Ma, Y. Dong, X. Zhou, Adv. Funct. Mater., 2017, **27**, 1704083.

16 H. Jiu, H. Wei, C. Wang, S. Che, Z. Guo, Y. Han, Q. Xu, X. Yu, L. Zhang, Int. J. Hydrogen Energy, 2022, **47**, 33719-33727.

17 M. Khalid, A. Honorato, H. Varela, L. Dai, Nano Energy, 2018, **45**, 127-135.

18 M. Ye, S. Li, X. Zhao, N. Tarakina, C. Teutloff, W. Chow, R. Bittl, A. Thomas, Adv. Mater., 2020, 32, 1903942.

19 Z. Xue, Y. Li, Y. Zhang, W. Geng, B. Jia, J. Tang, S. Bao, H. Wang, Y. Fan, Z. Wei, Z. Zhang, Z. Ke, G. Li, C. Su, Adv. Energy Mater., 2018, **8**, 1801564.

20 P. Thangavel, G. Kim, K. Kim, J. Mater. Chem. A, 2021, **9**, 14043-14051.

21 Z. Wang, J. Zhang, Q. Yu, H. Yang, X. Chen, X. Yuan, K. Huang, X. Xiong, Chem. Eng. J., 2021, **410**, 128366.

22 J. Xu, J. Li, D. Xiong, B. Zhang, Y. Liu, K. Wu, I. Amorim, W. Li, L. Liu, Chem. Sci., 2018, **9**, 3470-3476.